geosciences

MDPI

Article

Characterisation of Fault-Related Mn-Fe Striae on the Timpa Della Manca Fault (Mercure Basin, Southern Apennines, Italy)

Sabrina Nazzareni [1,*,†], Luciana Mantovani [1,†], Mattia Pizzati [1], Danilo Bersani [2], Tiziano Boschetti [1], Ambra Palmucci [3,4], Daniele Cirillo [3,5,*,†] and Francesco Brozzetti [3,5,†]

1 Department of Chemistry, Life Science and Sustainability, University of Parma, Parco Area delle Science 157/a, 43124 Parma, Italy; luciana.mantovani@unipr.it (L.M.); mattia.pizzati@unipr.it (M.P.); tiziano.boschetti@unipr.it (T.B.)
2 Department of Mathematical, Physical and Computer Sciences, University of Parma, Parco Area delle Science 7/a, 43124 Parma, Italy; danilo.bersani@unipr.it
3 CRUST—Centro inteRUniversitario per l'analisi Sismotettonica Tridimensionale, 66100 Chieti, Italy; ambra.palmucci@phd.unich.it (A.P.); francesco.brozzetti@unich.it (F.B.)
4 InGeo, University of Chieti-Pescara, 66100 Chieti, Italy
5 Laboratory of Structural Geology, 3D Digital Cartography and Geomatics, University of Chieti-Pescara, 66100 Chieti, Italy
* Correspondence: sabrina.nazzareni@unipr.it (S.N.); daniele.cirillo@unich.it (D.C.); Tel.: +39-(0)521-905333 (S.N.); +39-(0)85-355-8369 (D.C.)
† These authors contributed equally to this work.

Abstract: The Quaternary Mercure basin is a complex fault structure located in the Pollino region of the southern Apennines (Italy). A persistent seismic gap makes the Mercure basin structure one of Italy's highest seismic risk zones. The southernmost termination of the Mercure basin is the Timpa della Manca fault. The fault's mirror is characterised by distinctive, lineated, black-coloured striae decorating a cataclasite made of carbonate clasts. These black-coloured striae consist of a mixture of Mn phases, including hollandite, todorokite, birnessite, and orientite, which are associated with goethite and hematite along with minor amounts of phyllosilicates (chlorite, muscovite), quartz, and sursassite. This mineral association and their phase stability suggest that hydrothermal circulating fluids may have mobilised and re-precipitated low-temperature Mn hydrous phases within the shear zone, leaving remnants of higher-temperature minerals. Oceanic crust remnant blocks within the Frido Unit appear to be the most likely source of the Mn. The uniqueness of the Mn striae on the Timpa della Manca fault offers intriguing insights into fluid circulation within the Mercure basin tectonic system, with potential implications for the seismotectonic characteristics of the Pollino region.

Keywords: active fault; mineralisation on fault plane; earthquake; Calabria-Lucania Apennines manganese; oxides; XRD; Raman; fluid circulation

Citation: Nazzareni, S.; Mantovani, L.; Pizzati, M.; Bersani, D.; Boschetti, T.; Palmucci, A.; Cirillo, D.; Brozzetti, F. Characterisation of Fault-Related Mn-Fe Striae on the Timpa Della Manca Fault (Mercure Basin, Southern Apennines, Italy). *Geosciences* **2024**, *14*, 299. https://doi.org/10.3390/geosciences14110299

Academic Editor: Rosa Nappi

Received: 1 September 2024
Revised: 24 October 2024
Accepted: 3 November 2024
Published: 5 November 2024

1. Introduction

The southern Apennines are a Miocene–Pliocene thrust and fold belt currently influenced by a system of active and seismogenic extensional faults (Figure 1a). This "extensional belt", which trends WNW–ESE on average, is associated with a high seismic hazard, as demonstrated by significant earthquakes such as the 1980 Irpinia event (Mw 6.9) and the historic 1857 Basilicata earthquake (Mw 7.1) [1,2].

Within this framework, the Pollino region and the Mercure basin (Figure 1b) stand out as a persistent seismic gap despite being displaced by a complex array of Quaternary normal faults [3–5]. Historically, these areas have only experienced moderate magnitude earthquakes, including the 1998 Mercure earthquake (Mw 5.6 [6]) and the four-year-long 2010–2014 Pollino seismic sequence, (which peaked at Mw 5.2, [4,7]).

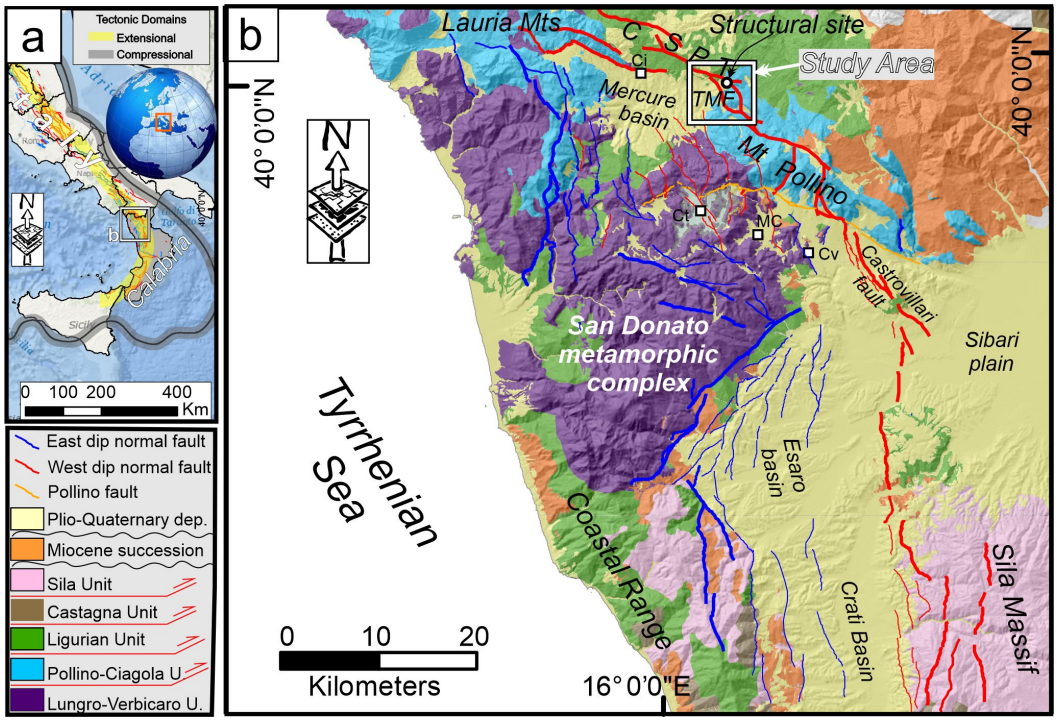

Figure 1. (**a**) Location map showing major tectonic domains in the southern Apennines of the Italian peninsula. The black rectangle indicates the location of the panel. The yellow stripe marks the active extensional domain, while the grey area represents the active frontal thrust domain. (**b**) Geological–structural map of the northern Calabria region, modified after Geological Map 25,000 scale of the Calabria region and from Lavecchia et al. [5] (Quaternary Faults). The black rectangle with a white border highlights the location of the studied area. The legend for the geological–structural map is provided in the left panel.

The primary normal faults in this region are well exposed with displacements exceeding 1 km. Most of these faults reveal free faces exhumed during the Late Quaternary. During the post-LGM (Last Glacial Maximum) period of approximately the last 18,000 years, their estimated slip rates range from 0.3 mm to over 1 mm per year [3,8].

The Timpa della Manca fault (TMF) marks the southernmost boundary of the tectonic structures bounding the Mercure Quaternary basin (Figures 1b and 2a). Like the northern and central structures of the basin, the TMF exhibits a well-exposed fault mirror that stretches continuously along several hundred meters with a displacement of at least 500 m. A distinctive feature of the TMF fault mirror is the presence of a black-coloured metallic coating on the lower part of the exposed surface (Figure 2b,c).

This lineated black-coloured coating on the TMF is unique, as it has not been documented on other fault planes in the region. Investigating the nature and structure of this coating is critical, as analysing its chemical and mineralogical composition could enhance the integration of kinematic and tectonic data, offering new insights into the evolution of Quaternary faults in the Apennines, which remain incompletely understood.

Characterising cataclasite generated by brittle deformation and the kinematic structures observed on the fault mirror provides valuable information about the deformation processes associated with slip events and the chemical reactions within the fault zone. This study analyses the TMF fault rocks and the Mn-Fe striae covering the fault at the Timpa della Manca site. The mineral composition of these black-coloured striae has been determined and their textural relationship with the surrounding host cataclasite has been carefully examined. Analysing the composition of the metallic coatings found on the recently unearthed part of the fault rocks could potentially lead to the development of new chemical investigation methods integrating structural geology surveys in the near future. These methods could be applied to this fault or others with similar features, contributing to

clarifying better the fracturing and exhumation processes along active fault planes. In turn, this could have important implications for evaluating seismic hazards in areas affected by extensional deformations.

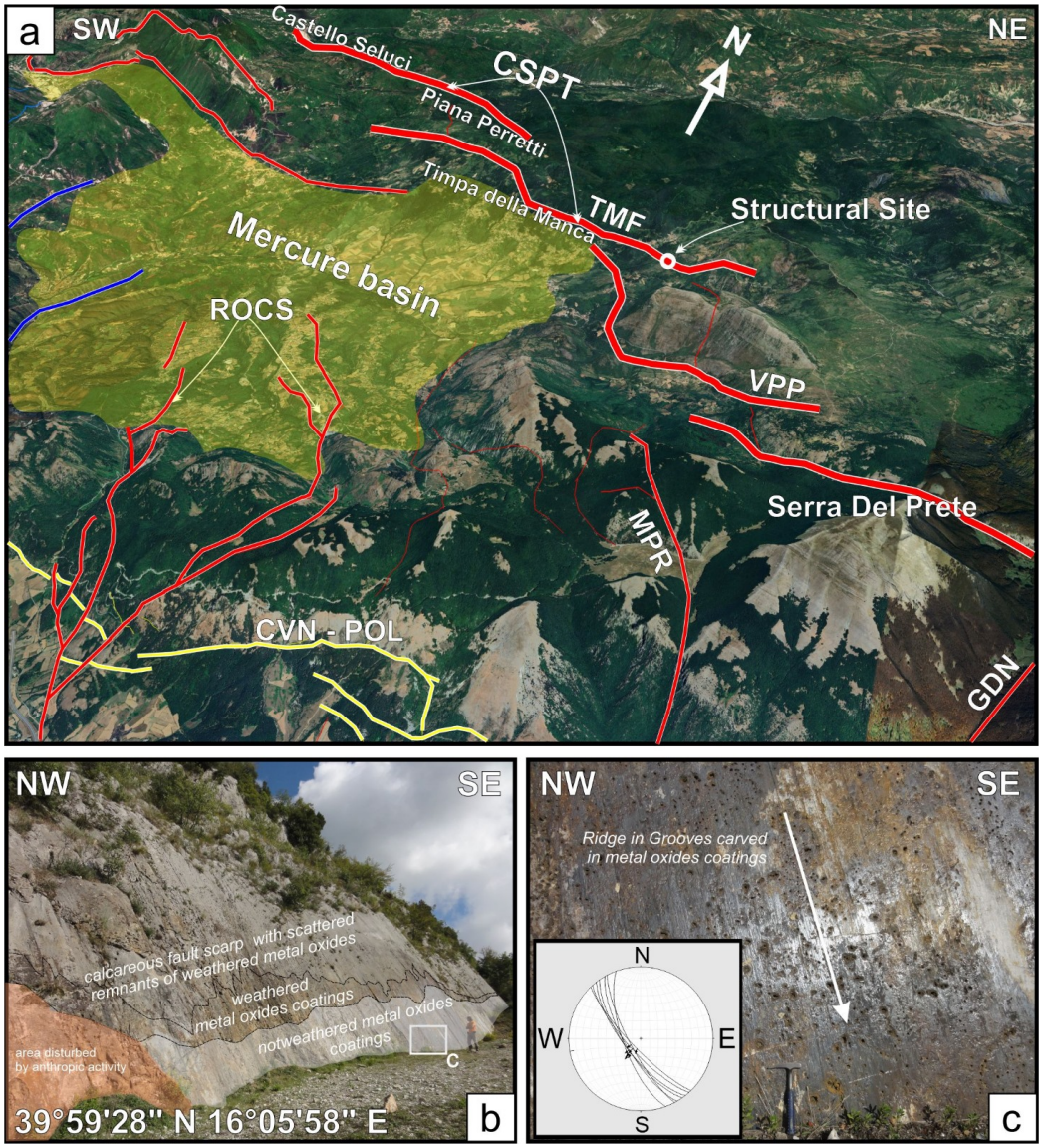

Figure 2. (**a**) Bird's-eye view of the active fault systems at the Calabrio–Lucania boundary. Red stripes indicate west-dipping normal faults (Catello Seluci–Piana Perretti–Timpa della Manca (CSPT); Viggianello–Prastio faults (VPP); Rotonda–Fosso Sambucoso faults (ROCS); Morano Calabro-Piani di Ruggio faults (MPR); Gaudolino fault (GDN)), blue stripes indicate east-dipping normal faults, and yellow stripes mark the SSW-dipping fault system of the Cozzo Vardo–Cozzo Nisco–Pollino (CVN-POL). The white circle highlights the structural site of the Timpa della Manca fault mirror (TMF) shown in panels (**b**,**c**), while the yellow area indicates the Mercure basin. The stereoplot in panel (**c**) represents structural data (fault planes and striae) collected along the outcropping fault in the study area.

2. Structural–Geological Setting

The Mercure basin is an intramountain tectonic depression located at the Calabria–Lucania boundary within the extensional belt of the southern Apennines. This belt is a regional system of NW–SE–striking Quaternary faults, which developed since the Early Pleistocene in the axial zone of the orogenic chain (Figure 1a). Some of these faults are currently active and capable of causing earthquakes [9–11]. The area of the Mercure basin (Figure 1b) is

characterised by both west-dipping and east-dipping normal faults. These fault systems extend through the Pollino massif and the San Donato metamorphic core towards the south, reaching into the Esaro and Crati valleys.

The filling of the basin is characterised by fluvial–lacustrine deposits of the Middle Pleistocene–Holocene age. Based on biostratigraphic data on syntectonic sediments [12,13] and radiometric determination on interbedded tephra layers [14], such dating constrains the timing of extensional tectonics in the area. The ages mentioned above align well with the beginning of normal faulting in nearby intramountain depressions, such as the Campotenese, Morano Calabro, and Castrovillari basins [15–17] located just south of the Mercure basin. Although some of the main extensional faults had been known for a long time, recent fieldwork [3] identified several other structures, most of which were previously unmapped (Figures 1b and 2a). An articulated horst and graben structure has been reconstructed for at least 60 km. The current activity of the Mercure basin boundary faults is supported by their clear connections to the recent instrumental seismic activity in the area over the last few decades. The 9 September 1998, Mw 5.6 Mercure earthquake was the strongest seismic event that hit the Southern Apennines after the 1980 Mw = 6.9 Irpinia earthquake.

Furthermore, the Rotonda–Pollino seismic sequence, which occurred between 2010 and 2014 and had a moderate magnitude (Mmax = 5.2), impacted the southern part of the Mercure basin with over 4000 events [4,7]. The 1998 and 2010–2014 seismic activity were linked with the west-dipping normal faults that define the basin's eastern boundary [3,6,18]. These faults are of considerable interest because they belong to a 40 km long active structural alignment including the Castrovillari fault (Figure 1b) to the south, which is recognised as capable of releasing earthquakes of up to M = 7.0 [19,20].

The Timpa Della Manca Fault

The Timpa della Manca fault segment (TMF, Figures 1b and 2a) is one of the most prominent structures bounding the Mercure Quaternary basin. In the field, its trace is marked by fault mirrors and fresh scarps, which are well exposed along the south-eastern side of the basin (Figure 2b,c).

This segment is the southernmost of the 18 km long Castello Seluci–Piana Perretti–Timpa della Manca fault (CSPT, Figures 1b and 2a), which juxtaposes the Meso-Cenozoic shallow water carbonates with pillow basalt intrusions of the Apennines Platform with Miocene flysch-type deposits and the overlying tectonic melange complex of the Frido Unit [21,22]. The latter consists of an allochton chaotic metasedimentary assemblage containing blocks of oceanic and continental crust, formed in the Cretaceous–Eocene accretionary prism and later exhumed and transported above the external Apennines units [23,24].

The CSPT fault shows an average strike of N120°–125° and dips 50°–70° to the SSW. Near its northern and southern tips, there are some changes in direction towards NNW—SSE trends. The displacement associated with the fault varies along its length, with the maximum values found in the northwestern segment (north of Castelluccio Inferiore, see Figure 1b) and the southern segment of Timpa della Manca, where it exceeds 500 m. Conversely, the fault displacement decreases noticeably in the central sector at a right-lateral step-over.

The TMF's studied outcrop (white square in Figure 1b, white circle in Figure 2a) is a fault scarp that reaches heights of up to 15 m and extends along the strike for several hundred meters in the field (Figure 2a,b).

The fault rock's texture is characterised by a tightly cemented fine-grained breccia mainly made of millimeter-sized carbonatic clasts interspersed in a finer matrix, with a calcareous composition. The upper portion of the scarp is strongly weathered and displays an irregular erosion profile with remnants of slickensides on Cretaceous limestones alternating with deeply karstified sectors (Figure 2b). This upper scarp lacks clear kinematic

indicators due to significant erosion or dissolution of the main slip surface. However, occasional remnants of highly weathered black oxides are still detectable.

The lower portion of the scarp corresponds to a fresh free face which represents the part of the fault that was unearthed during recent co-seismic exhumation events (Figure 2b). At the surface, the free face appears as a polished slickenside characterised by a strongly oriented mm-scale lineation of ridge-in-grooves type and, on a larger scale, by fault mullions some tens of cm wide (Figure 2b, detail in Figure 2c). Both the grooves and mullions indicate nearly pure dip-slip kinematics (see stereo plot inset in (Figure 2c), consistent with the extensional stress field that has been active in the area since at least the Middle Pleistocene (the last 800 ka, [6,8]).

The lower scarp of TMF appears uniformly covered by a well-preserved black metal oxide coating that has not been weathered and is easily identifiable thanks to its characteristic glossy appearance. Ridge-in-groove lineation is also carved in this metal pellicle suggesting that the precipitation of the latter occurred before the movements that produced the lineation. An intermediate band marks the transition from the lower to the upper part of the scarp. The band has a continuous coating of metal oxides, but it appears weathered and oxidised, with a "rusty" appearance (Figure 2b).

3. Data and Methods

3.1. Analysed Sample

Carbonate fault rock hosting Mn-rich striae was saw-cut, and a polished, 30 µm thick, petrographic thin section was carried out at the Department of SCVSA (University of Parma). Both the chemistry and texture of the cataclasite and the dark mineralised striae have been investigated. Sample amounts to be dedicated to chemical and mineralogical analyses were collected directly from the Mn-striae hand sample.

3.2. Microstructural Observations by Optical Microscopy and Cathodoluminescence

Optical microscopy and microstructural analyses were performed using a Nikon Super-CoolScan 5000 high-resolution thin-section scan, while fault rock details were acquired with a Zeiss Axioplan2 standard, transmitted light, petrographic microscope coupled with a Leica DC120M camera at the Department of SCVSA (University of Parma). Details concerning the fault rock microstructure and carbonate cement texture-pattern were acquired with a CITL CL 8200 Mk2-5 cold cathodoluminescence apparatus at the Department of SCVSA (University of Parma). The instrument was coupled with a Leica DM2700P standard petrographic transmitted light petrography microscope, which was equipped with a Leica DFC450C high-sensitivity camera, specifically designed to work on low-luminescence samples.

Cathodoluminescence image acquisition was performed under controlled vacuum conditions of 0.02–0.04 mbar, with an electric current producing the electron beam to induce the luminescence in the sample set to 10 kV and 240–260 µA. Photomicrographs were acquired using both transmitted light and cathodoluminescence, with the camera exposure time set to 25–30 ms for transmitted light and 10 s for cathodoluminescence, respectively.

3.3. SEM

Fragments of the cataclastic fault rocks were handpicked and analysed using a scanning electron microscope (SEM) Jeol 6400 equipped with an Oxford energy-dispersive system (EDS) microprobe at the Department of SCVSA (University of Parma). The operative conditions were 15 kV, 1.2 mA current, a 1 µm beam diameter, and a counting time of 75 s. An average of 5–10 analytical points per sample were taken, to assess the compositional variability. SEM images were acquired using both secondary and back-scattered electron detectors and the samples were observed in their natural state, deposited on a tape layer, and coated with graphite.

3.4. Powder X-Ray Diffraction

Mineralisation present along the fault has been selected and removed for the measurements. Small amounts of mineralised material have been grinded to fine-grained powder for mineralogical characterisation by using X-ray diffraction analysis [25].

To remove the carbonate component, the black-coloured material has been treated in HCl 0.1 mole and successively analysed by powder XRD. Measurements have been carried out using a Bruker D2 Phaser powder diffractometer at the Department of SCVSA (University of Parma). The instrument operated at 30 kV and 10 mA, utilising Cu Kα radiation (λ = 1.54178 Å). Data acquisition covered the 5–80° 2θ range, with a step size of 0.02° and a counting time of 1 s per each step. Samples were spun at 30 rpm during measurement. For qualitative analysis, major crystalline phases were identified using EVA software (Bruker EVA, 2018) with the Crystallography Open Database (COD). The detection limit of the instrument is ca. 1–2 wt%.

3.5. Micro-Raman

Raman spectroscopy measurements have been carried out at the Department of MPCS (University of Parma). Non-polarized Raman spectra were recorded in a nearly backscattering geometry with a Horiba LabRam microspectrometer equipped with an integrated Olympus BX40 microscope, a He-Ne laser (632.8 nm) and a Nd:YAG laser (473.1nm). The spectral resolution was about 2 cm^{-1}. The power on the sample was kept below 10 mW using neutral density filters. A microscope with 100× and 50× ultra-long-working-distance objectives was used to collect the Raman signal. Before each measurement session, the spectral position was calibrated using the Raman bands of silicon, aragonite and polystyrene, depending on the spectral range.

3.6. Thermodynamic Calculation

The Act2 tool of the software suite The Geochemist's Workbench (GWB, version 7.0.6, build 2878; [26]) was used to construct the Eh-pH diagrams at different temperatures and under isobaric conditions typical of the transition between the continental shelf and the abyssal zone (P = 350 bar).

The UNITHERM thermodynamic database, version 4.4, and the UT2K converter [27], along with the K2GWB software (version 2005) [28], were employed to generate the initial dataset in the GWB format. Given the lack of thermodynamic data concerning manganese silicates such as orientite and sursassite, both in thermodynamic databases and in the literature, this study utilized the braunite data from Robie et al. [29]. For bixbyite, hausmannite, manganosite, and pyrolusite, the data published by Jacob et al. [30,31] were used.

The Gibbs free energy of formation (ΔG°f) values for birnessite and todorokite were obtained from the data0.cmp database of the EQ3/6 software, version 8.0 [32], while the other thermodynamic parameters such as enthalpies of formation, entropies, and heat capacities (ΔH°f, S°, C°p) were inferred from the HSC Chemistry® software, version 7.193 [33].

Furthermore, additional data for dissolved species not included in UNITHERM were extracted from both the slop07.dat (https://search.asu.edu/profile/388445; https://reaktoro.org/v1/thermodynamic-databases.html (accessed on 10 July 2024)) and the THERMODDEM datasets [34]. The solubility and hydrolysis data of solid and liquid species at different temperatures, expressed as logK, were calculated using OrganoBioGeoTherm software, version 1.52 (OBGT) and a Windows interface of SUPCRT [35] and then manually entered into the final thermodynamic database for the GWB.

4. Results

4.1. Microstructural Features of the Fault Rock

The studied fault rock shows a cataclastic texture with carbonate clasts having different sizes and shapes dispersed in a fine-grained matrix (Figure 3a). The brown to black-

coloured Mn-oxide striae layer is 2–3 mm-thick and displays a sharp contact with the host fault rock (Figure 3b).

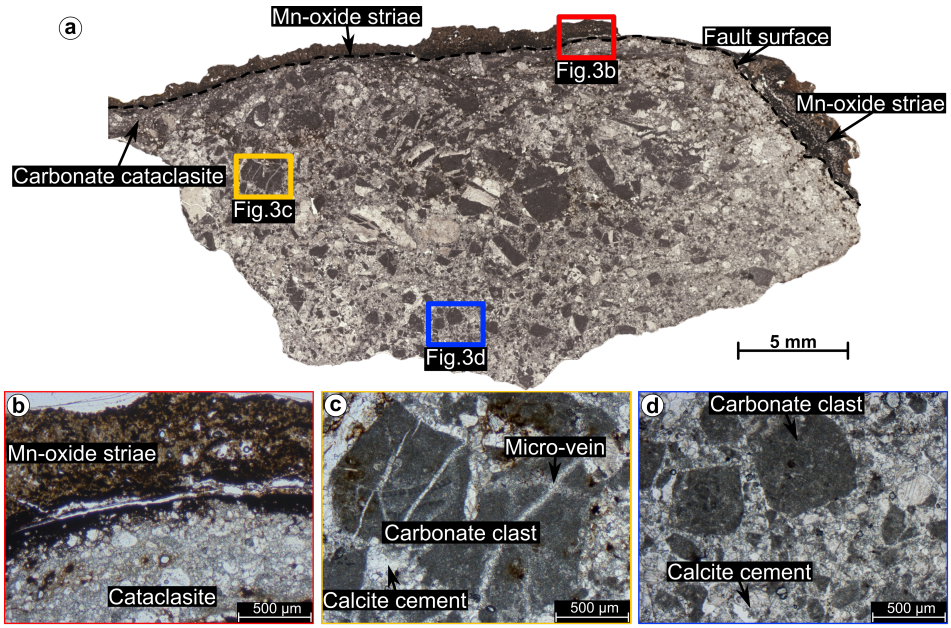

Figure 3. Microstructural details of the studied Mn-oxide fault striae. (**a**) Thin-section, high-resolution scan showing the Mn-oxide fault striae to the top and right-hand side of the figure. (**b**) Detail of the fault surface decorated with the dark brown Mn-oxide striae. (**c**) Coarse-grained carbonate clast displaying calcite micro veins. (**d**) Detail of the bulk carbonate cataclasite hosting the Mn-oxide fault striae.

At the millimetric scale, the bulk framework of the fault rock is composed of dark grey to black-coloured carbonate clasts with equivalent diameters up to 1 mm. However, in the central portion of the thin section, a few coarser and angular clasts are present with equivalent diameters up to 2–3 mm (Figure 3c), describing a texture similar to a proto-cataclasite or an immature cataclasite. Moreover, clast size becomes progressively coarser and more preserved away from the boundary between the Mn-rich striae and the host carbonate cataclasite, describing a marked clast comminution gradient. A few coarse-grained clasts are characterized by the presence of calcite micro-veins (<50 µm aperture), with different orientations (Figure 3c).

Along the entire thin section, most of the former pore space has been filled by precipitation of calcite cement (Figure 3d), with carbonate clasts acting as cementation nuclei. Under cathodoluminescence, the Mn-rich striae appear dark brown to black at contact with the carbonate cataclasite, while they become light brown moving away from the boundary (Figure 4a).

Fine-grained and rounded carbonate clasts have been found within the Mn-oxide striae. The carbonate cataclasite near the boundary with the Mn-rich striae is fine-grained and underwent a pervasive process of healing by calcite precipitation in the former pore space, sealing almost completely the porosity. Calcite cement displays crystal size below 30–40 µm. It can be easily recognized under cathodoluminescence by the slightly brighter orange colour than the brown/dull orange characterizing the carbonate clasts (Figure 4a). In the central portion of the thin section, clasts display a coarser particle size and more angular, rougher outer boundaries. The areal ratio between calcite cement and clasts is higher compared to the striae–cataclasite boundary, and cement crystal size is coarser (50–150 µm) (Figure 4b).

Calcite crystals display well-developed zonation rims made of alternated dull and bright concentric zones. Cementation is not as pervasive as in the vicinity of the Mn-rich striae, leaving a patchily distributed porosity (Figure 4b). Far away from the Mn-rich striae,

the areal amount of carbonate clasts is lower, and the fault rock overall texture is dominated by the presence of zoned calcite cement with crystal size up to 200–300 µm (Figure 4c).

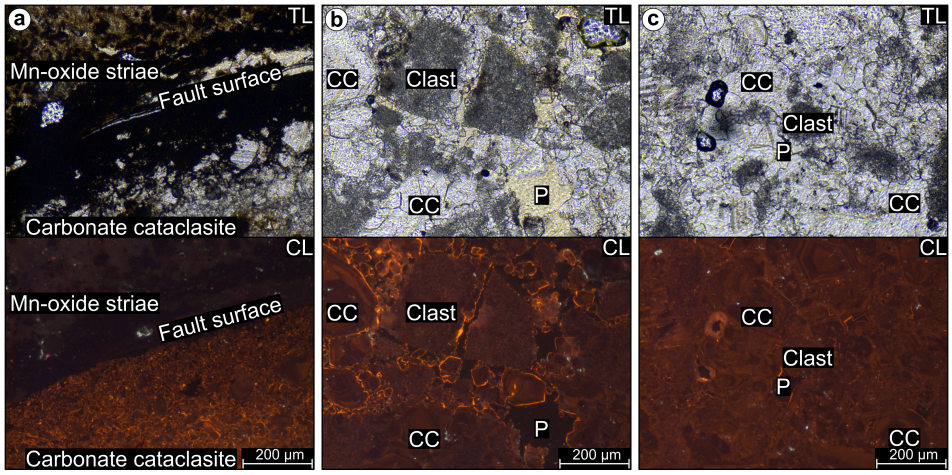

Figure 4. Transmitted light (TL) and cold cathodoluminescence (CL) photomicrographs of the Mn-oxide striae and of the host cataclasite. (**a**) Detail showing the fault surface with the Mn-oxide striae. (**b**) Fault cataclasite with fragmented carbonate clasts and porosity (P) partially filled with calcite cements (CCs). (**c**) Detail of host cataclasite acquired 3 cm away from the Mn-oxide striae, showing the dominance of zoned calcite cement with few carbonate clasts.

4.2. Chemical and Structural Characterisation

Calcite is the main mineral in the cataclasite, together with quartz, but nearly idiomorphic sheet silicates from the chlorite family were also identified. The brown and black-coloured striae material was found to be a mix of manganese oxide–hydroxide and silicate phases (e.g., orientite), as well as Fe oxide–hydroxide (e.g., goethite) in a fine intergrown texture. Furthermore, the presence of Ba and Mn together suggests the occurrence of hollandite (Figure 5). Table 1 displays the chemistry of the phases analysed by SEM-EDS.

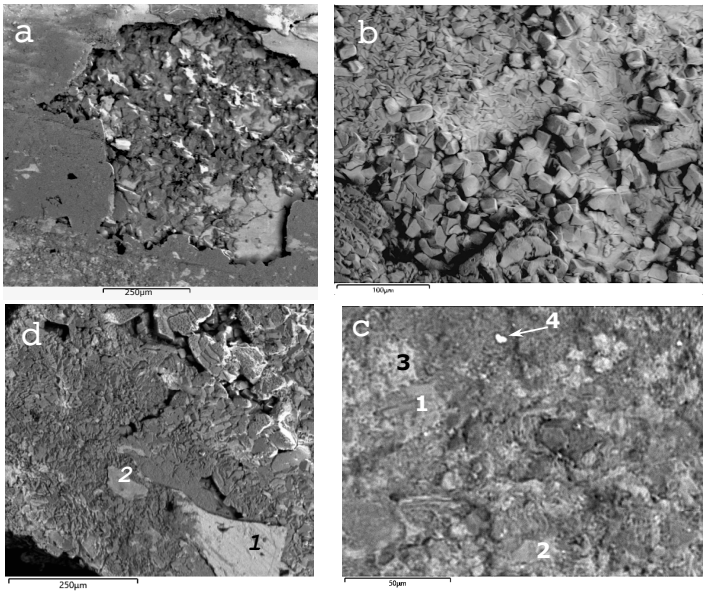

Figure 5. Secondary electrons images of the studied cataclasite. (**a**) Black cataclasite striae scale; (**b**) particular of calcite crystals; (**c**) particular of the mixed texture of calcite (dark gray), orientite (1) and hollandite (2) with other Mn-Fe (hydro)oxides (3), and the presence of barite (4); (**d**) detail of the Mn-phase striae with hollandite (1) and sursassite (2) crystals. See text for discussion.

Table 1. SEM-EDS chemical composition of phases from different portions of the Mn striae shown in Figure 5. Mixed and intergrown compositions are reported.

Elements	Sursassite	Hollandite	Barite+ Calcite	Mix Mn-FePhases	Orientite	Chlorite
O	41.11	27.76	29.07	32.14	32.84	46.39
Mg	1.81	1.35		1.67	3.28	14.86
Al	15.09	4.43	0.86	3.69	7.59	5.76
Si	16.46	4.99	1.55	7.45	7.61	24.69
S			3.38			
K	0.86	0.55			1.12	
Ca	3.5	2.36	49.14	3.21	7.71	7.04
Ti					0.43	
Mn	21.15	41.53		22.96	37.43	
Fe		6.74		25.35	1.4	1.25
Ni					0.57	
Ba		10.3	16	3.54		
Total	100	100	100	100	100	100

The thickness and strong intergrowth of the Mn-rich striae with the cataclasite rocks complicated the XRD identification of Mn and Fe phases. To avoid calcite saturation in the XRD pattern, we sampled a small portion of the Mn-rich striae and after a manual removal of calcite, quartz was the only sialic phase identified in the powder XRD pattern (Figure 6a) exhibiting well-defined and sharp peaks.

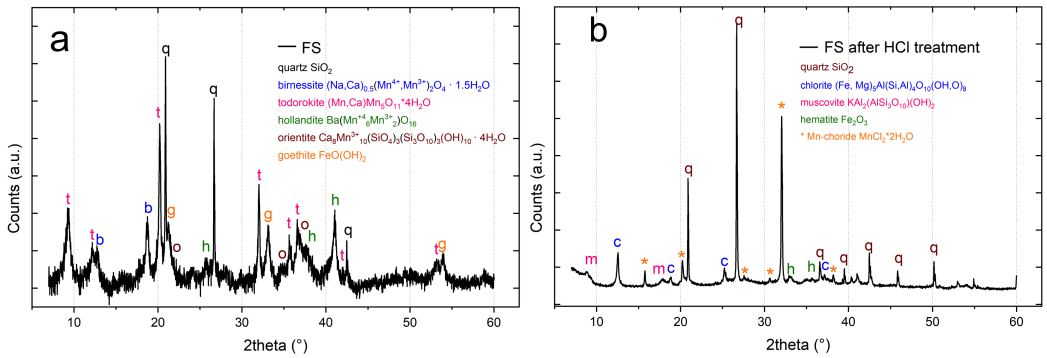

Figure 6. (**a**) XRD powder diffraction pattern of the Mn-Fe phase striae; (**b**) XRD powder diffraction pattern of the Mn-Fe phase striae after acid attack.

The Mn and Fe phases identified by XRD (Figure 6a) include:

- Birnessite ($(Na,Ca)_{0.5}(Mn^{+4},Mn^{+3})_2)O_4$ 1.5 H_2O).
- Todorokite ($(Na,Ca,K,Ba,Sr)_{1-x}$ $(Mn,Mg,Al)_6O_{12}$ 3-4 H_2O).
- Hollandite ($Ba(Mn^{+4}{}_6Mn^{+3}{}_2)O_{16}$).
- Orientite ($Ca_8Mn^{+3}{}_{10}(SiO_4)_3(Si_3O_{10})_3(OH)_{10}$ 4 H_2O).
- Goethite $Fe^{+3}O(OH)$.

In the specimen treated with HCl, quartz, chlorite, muscovite, and hematite were identified (Figure 6b). A hydrous Mn-chloride was also detected in the XRD pattern, likely formed by the reaction of HCl with the Mn- oxide–hydroxide previously present in the striae. Manganese phases are often poorly crystalline, and intergrowth between different phases is common [36,37], making identification by XRD complex. To add more constraints in phase identification, Raman spectra were measured on the thin section of Mn-rich striae and cataclasite rock. The spectra measured in the Mn-rich striae are characterised by broad bands between 400 and 700 cm^{-1}, suggesting poor crystallinity and probably a mixture of Mn phases (Figure 7).

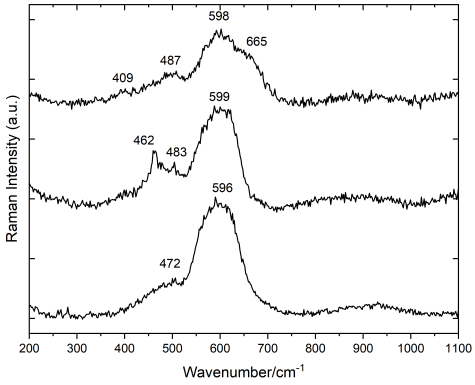

Figure 7. Raman spectra of the Mn-rich striae. See text for discussion.

The identification of Mn phases by Raman spectroscopy is not trivial either; although these bands can be assigned to oxy-hydroxide Mn phases (Table 2), the individual minerals observed by XRD could not be clearly identified. The presence of goethite was also detected.

Table 2. Raman frequencies (in cm^{-1}) of the Mn-phases.

Sample Point	Frequencies					
S2	488.8		598.4	665.0	905.9	1085.6
S5	483.7		599.0	609.9		
S8	483.4	583.7	596.0	628.3	946.9	

Thermodynamic calculations were performed to define the stability of Mn phases detected in the striae. The lack of thermodynamic data concerning manganese silicates such as orientite and sursassite was supplied using braunite data. The Eh-pH diagrams in Figure 8 show the variation in stability fields of the Mn phases, suggesting that the association between manganese oxides (birnessite, todorokite, and pyrolusite as a substitute for hollandite) and braunite below 150 °C is more similar to the observed TMF striae assemblage. Above 150 °C, the stability fields of birnessite and todorokite tend to decrease significantly until they disappear.

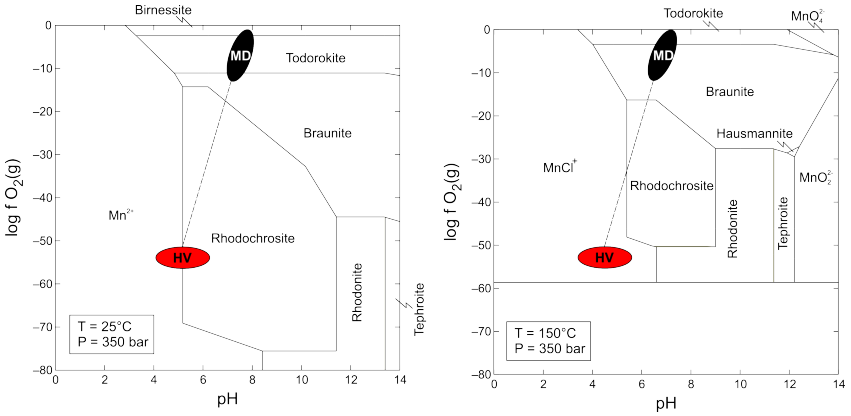

Figure 8. Oxygen fugacity logf(O_2) versus pH of the system Mn, Fe, C, Cl, and Si. Dissolved silica and Fe were saturated in quartz and hematite, respectively. Activities and fugacities of other species were log[Mn] = −3, logf(CO_2) = −1.5, log[Cl^{-1}] = −0.5. The stability field of pyrolusite, which lies just above birnessite and todorokite, was disabled. HV-red and MD-black fields represent the mean physico-chemical conditions of hydrothermal vents and mixed (dashed line) hydrothermal oceanic fluids that deposited Mn oxides and silicates.

5. Discussion

Metal oxy-hydroxide striae are not common on fault planes; nevertheless, the formation of mineral deposits associated with fault activity is well known (e.g., mesothermal and ephithermal lode-gold deposits such as Carlin-type and Jacobina deposits or Mississippi Valley-type Zn-Pb deposits). The occurrence of metal oxide fillings or diagenetic concretions within brittle fractures or fault zones has been documented in the literature [38–41].

These features are commonly associated with the role played by fault rocks in promoting the flow of mineralising fluids [39,42]. Manganese is uncommon in fault-related mineralisations, but Spencer and Welty [40] reported the mobilisation of Mn (and Fe) by hydrothermal fluids that transported Mn to the surface through the Buckskin-Rawhide detachment fault (lower Colorado river).

The wide geological availability of Mn, which is second only to Fe in abundance among the heavy metals, and the ability of Mn to exist in three oxidation states (+2, +3, +4), allow the formation of Mn minerals under a wide range of chemical and temperature conditions. Manganese and iron have similar geochemical behaviour, but they differ in solubility, with Mn more soluble than Fe: on cooling, a hydrothermal solution decreases acidity, precipitating iron, while Mn remains in solution, reaching a shallower level [43,44].

Moreover, manganese phase stability strongly depends on the redox potential, and solubility changes with the oxidation state (Mn^{2+} oxides are soluble, Mn^{3+} and Mn^{4+} hydro-oxides are insoluble). Consequently, surface water and groundwater interaction with rock containing Mn minerals can easily mobilise and transport Mn in solution.

The black-coloured striae coating the TMF plane resulted in a mixture of manganese oxy-hydroxide and silicate with minor iron oxy-hydroxide. Quartz, barite, chlorite, and muscovite were also detected (Table1, Figures 5 and 6). Manganese phases typically occur as a poorly crystalline, fine-grained mixture of several phases, making their identification by XRD and Raman difficult.

Moreover, the Raman spectra of several Mn phases are very similar, making rather challenging their identification. In addition, decomposition processes and phase transformations may occur during Raman measurements, for this reason we carefully used a low laser excitation power and checked the Raman spectra evolution during measurements. No spectra changes were detected, and we can reasonably assert that no Mn-phase transformation occurred during the measurements. Nevertheless, the combination of low crystallinity and fine-grained mixture of different phases prevented to assign convincing Raman spectra to single Mn phases.

In fact, most Mn oxy-hydroxides exhibit prominent bands at approximately 630 cm^{-1} and 580 cm^{-1} [45–47], as well as weaker bands at lower wavenumbers (Table 2). However, the low crystallinity, which corresponds to broad band widths, makes it challenging to determine the precise composition of the mixture.

A mixture of Mn oxide (hollandite), Mn hydroxide (todorokite, birnessite), and Mn silicate (orientite) was identified by XRD. However, SEM analysis suggests the presence of sursassite ($(Mn^{+2}, Ca)_2\ Al_2(Al, Fe^{+3}, Mn^{+3}, Mg)(SiO_4)(Si_3O_7)(OH)_3$), indicating that other Mn phases may not have been identified (Table 1).

Todorokite and birnessite are the most common minerals in soils (together with hollandite, vernadite and lithiophorite), sediments and oceanic manganese nodules [36,48,49]. They are also important components in desert varnishes, Mn coating and dendrites [36,37]. Todorokite, birnessite and orientite are commonly found as alteration products of primary ores, being low temperature replacement minerals of manganese oxide and oxysalt.

Structural arrangements of the Mn-oxide building block (MnO_6 octahedron) can be modulated in different chains (or tunnels) or layer structures. Water molecules are located in the tunnels or in the interlayer.

Despite the structural arrangements, hollandite and todorokite, which are tunnel Mn oxides, can both have fibrous morphology. Instead, birnessite and orientite are layered (sheet) Mn oxide and silicate, respectively [36,37] with a layer morphology. Pressure and

temperature stability, compressibility (bulk modulus) and morphology of the Mn phases can influence their occurrence as striae in a fault plane.

The identified Mn oxides are low-temperature (<200–300 °C) phases compatible with fluids circulating in a shallow-depth portion of a fault zone, while the layered morphology may favour their growth (and stability) under oriented shear stress. In fact, sheet minerals may have anisotropic compressional behaviour (i.e., gypsum [50], phase-X [51], birnessite [52]) that can favour the crystallisation of oriented microstructure more able to survive under the applied stress. Birnessite is stable up to 0.19 GPa (equivalent to circa 5 km depth) under cold subduction gradient [52], at higher pressure it transforms into the super-hydrous phase buserite. The literature data on the compressibility behaviour of the other Mn oxides are lacking, but hollandite-like structure is known to be stable at mantle pressure conditions [53].

It seems that the Mn oxides dissolved and re-precipitated at depth before the fault plane was exposed at the surface. The presence of striae carving the coating (Figures 2 and 5) clearly indicates that the slip occurred after their precipitation. These observations suggest that the fault-slip directly caused the exhumation of the free face but are not enough evidence to prove that it occurred during an earthquake.

However, the observation on the fault shows that the striated oxide coverage exhibits progressively decreasing alteration conditions from bottom to top (Figure 2), with rather abrupt variations. This supports the hypothesis that they may correspond to co-seismic exhumations. The bands inside these rocks appear to be uniformly weathered, suggesting that they could be sections of the fault that were quickly exposed during surficial deformation associated with earthquakes. This means they would have been evenly exposed to the atmospheric agents for the same amount of time. Such a peculiar characteristic could help in identifying the co-seismic displacement related to pre-historic earthquakes in the absence of other more robust fault activity indicators (cosmogenic radionuclides, dating of down-thrown Holocene deposits in the hanging wall block).

Our research primarily focuses on characterizing the nature of the oxide coating on the fault. Therefore, no definitive answer to a seismological question is claimed in this study. Thorough paleo-seismological investigations conducted with appropriate methodologies combining structural geology, Quaternary geology and seismology [54,55] are deemed necessary and the outcrop studied on the TMF can be considered as an ideal for further research. Nonetheless, this work could serve as a stimulus for future paleo-seismological studies aimed at better defining and constraining the present-day seismic hazard of the Pollino area.

The calcite of the TMF fault rock comes from the footwall carbonate unit, but the mineral assemblage found in the black-coloured striae needs a different source. Mn-oxides, goethite and hematite, chlorite and muscovite suggest a mafic source possibly associated with the metasedimentary oceanic crust present in the Frido Unit. In fact, Mn (and Fe) mineralisations occur in the ocean floor (nodules, micro-concretions, coatings and crust) and are also present in volcanic massive sulphide (VMS) deposits. For example, a paragenesis of Mn oxides with sursassite (and chlorite) is compatible with VMS mineralisations like those of the Molinello and Gambatesa mines, (Liguria, Italy [56]).

Nevertheless, in the nearby Terranova del Pollino location, Mongelli et al. [57] reported the presence of Fe-(siderite) and Mn-carbonate (rhodochrosite) layers intercalated with shales in the tectonic melange (dated Cretaceous–Late Miocene) above the Frido Unit in the Northern-Calabrian Unit. Such diagenetic mineral masses could represent the primary source of Mn and Fe. The fault zone itself could have behaved as a preferential conduit towards deep-seated fluids, driving them upward during seismic events, according to the seismic pumping model [58,59]. Fluid upwelling in cohesive rocks is particularly favoured along the highly fractured and permeable damage zone [58]. Following this, the origin of Mn-rich striae may be related to the precipitation from saturated fluids during co-seismic or interseismic fault activity intervals. The thermodynamic calculations suggest a temperature below 150 °C for the the association between Mn oxides and Mn silicate.

Moreover, compared to the average pH and log(f)(O_2) values of hydrothermal fluids (pH = 5; log(f)(O_2) = −55; [60], these conditions seem to be favoured by more oxidizing conditions with a pH slightly lower than 8, not dissimilar from those of post-Cretaceous oceanic conditions [61]. This, therefore, could suggest a mixing between hydrothermal fluids and ocean water (Figure 8). Additionally, the presence of rhodochrosite above the Frido unit could indicate a different stage of mixing at lower redox potentials. However, at the moment, we cannot better constrain the source of manganese from the Frido Unit or the tectonic melange.

6. Conclusions

The TMF fault mirror is characterized by distinctive, lineated Mn striae that coat a cataclasite made of carbonate clasts. Calcite cement precipitated in the available pore space of the cataclasite, progressively sealing porosity towards the fault mirror, which suggests fluid circulation.

The black-coloured striae consist of a mixture of Mn phases (hollandite, todorokite, birnessite, orientite) associated with goethite and hematite. The presence of a mineral from the chlorite family, along with muscovite, quartz, and sursassite, suggests a mafic source for the mineralization.

The TMF structure juxtaposes Meso-Cenozoic carbonates with Miocene flysch-type deposits and with an allochthonous chaotic metasedimentary melange of the Frido Unit. Oceanic crust blocks contained within the Frido Unit appear to be a likely source of the Mn.

The circulation of hydrothermal fluids may have mobilized and re-precipitated the low-temperature Mn hydrous phases within the fault zone, leaving remnants of higher-temperature minerals. The uniqueness of the Mn striae on the TMF plane offers intriguing insights into fluid circulation within the Mercure basin tectonic system [62], with potential implications for the seismotectonics of the Pollino region. It is evident that this circulation of Fe-Mn-enriched fluids must have occurred after the Frido Unit was downthrown and placed in lateral contact with the Meso-Cenozoic carbonates of the Apennine platform due to extensional tectonics. Considering the chronostratigraphic constraints on the onset of extensional tectonics in this segment of the chain [3,4], this process can be attributed to the Middle Pleistocene to the present. This deduction suggests that the deposition of the coatings and the formation of the striae are related to the Quaternary activity of the fault, but not necessarily directly associated with coseismic rupture processes.

Our work provides additional insights into the interactions between active tectonics and fluid geochemistry, which warrant further investigation to achieve a more comprehensive understanding of the seismotectonic framework in the Calabria–Lucania boundary area. In conclusion, this work could serve as a foundation for future studies, particularly in advancing the understanding of fluid circulation in various tectonic settings such as the Italian Apennines chain [63–65] and worldwide context [40,66]. The findings provide valuable insights that may inspire further research into the interplay between fluid dynamics, structural evolution in active fault systems and their interaction with fault planes and associated mineralizations.

Author Contributions: Conceptualization, S.N., F.B. and D.C.; methodology, S.N., L.M., F.B. and M.P.; software, L.M., T.B. and D.C.; validation, S.N., F.B. and D.C.; formal analysis, S.N., L.M., F.B. and M.P.; investigation, S.N., L.M., F.B., M.P. and D.C.; data curation, S.N., L.M., M.P., D.B., T.B., A.P. and D.C. writing—original draft preparation, S.N., L.M., F.B. and M.P.; writing—review and editing, S.N., L.M., F.B., M.P. and D.C.; supervision, S.N., F.B. and D.C.; funding acquisition, L.M. and F.B. All authors have read and agreed to the published version of the manuscript.

Funding: This work has benefited from the equipment and framework of the COMP-HUB and COMP-R Initiatives, funded by the 'Departments of Excellence' program of the Italian Ministry for University and Research (MIUR, 2018-2022 and MUR, 2023-2027). This research was funded by DiSPUTer Departmental Research grants 2021 (Resp. F. Brozzetti).

Data Availability Statement: XRD and Raman data are available upon request from the authors

Acknowledgments: Anonymous referees are greatly acknowledged for improving the manuscript.

Conflicts of Interest: The authors declare no conflicts of interest.

References

1. Bello, S.; de Nardis, R.; Scarpa, R.; Brozzetti, F.; Cirillo, D.; Ferrarini, F.; Di Lieto, B.; Arrowsmith, R.J.; Lavecchia, G. Fault pattern and seismotectonic style of the Campania–Lucania 1980 earthquake (Mw 6.9, Southern Italy): New multidisciplinary constraints. *Front. Earth Sci.* **2021**, *8*, 608063. [CrossRef]
2. Bello, S.; Lavecchia, G.; Andrenacci, C.; Ercoli, M.; Cirillo, D.; Carboni, F.; Barchi, M.R.; Brozzetti, F. Complex trans-ridge normal faults controlling large earthquakes. *Sci. Rep.* **2022**, *12*, 10676. [CrossRef] [PubMed]
3. Brozzetti, F.; Cirillo, D.; de Nardis, R.; Cardinali, M.; Lavecchia, G.; Orecchio, B.; Presti, D.; Totaro, C. Newly identified active faults in the Pollino seismic gap, southern Italy, and their seismotectonic significance. *J. Struct. Geol.* **2017**, *94*, 13–31. [CrossRef]
4. Cirillo, D.; Totaro, C.; Lavecchia, G.; Orecchio, B.; de Nardis, R.; Presti, D.; Ferrarini, F.; Bello, S.; Brozzetti, F. Structural complexities and tectonic barriers controlling recent seismic activity of the Pollino area (Calabria-Lucania, Southern Italy)–constraints from stress inversion and 3D fault model building. *Solid Earth Discuss.* **2021**, *13*, 205–228. [CrossRef]
5. Lavecchia, G.; Bello, S.; Andrenacci, C.; Cirillo, D.; Pietrolungo, F.; Talone, D.; Ferrarini, F.; de Nardis, R.; Galli, P.; Faure Walker, J.; et al. QUIN 2.0-new release of the QUaternary fault strain INdicators database from the Southern Apennines of Italy. *Sci. Data* **2024**, *11*, 189. [CrossRef]
6. Brozzetti, F.; Lavecchia, G.; Mancini, G.; Milana, G.; Cardinali, M. Analysis of the 9 September 1998 Mw 5.6 Mercure earthquake sequence (Southern Apennines, Italy): A multidisciplinary approach. *Tectonophysics* **2009**, *476*, 210–225. [CrossRef]
7. Totaro, C.; Seeber, L.; Waldhauser, F.; Steckler, M.; Gervasi, A.; Guerra, I.; Orecchio, B.; Presti, D. An intense earthquake swarm in the southernmost Apennines: Fault architecture from high-resolution hypocenters and focal mechanisms. *Bull. Seismol. Soc. Am.* **2015**, *105*, 3121–3128. [CrossRef]
8. Papanikolaou, I.D.; Roberts, G.P. Geometry, kinematics and deformation rates along the active normal fault system in the southern Apennines: Implications for fault growth. *J. Struct. Geol.* **2007**, *29*, 166–188. [CrossRef]
9. Brozzetti, F. The Campania-Lucania Extensional Fault System, southern Italy: A suggestion for a uniform model of active extension in the Italian Apennines. *Tectonics* **2011**, *30(5)* . [CrossRef]
10. Lavecchia, G.; Ferrarini, F.; Brozzetti, F.; De Nardis, R.; Boncio, P.; Chiaraluce, L. From surface geology to aftershock analysis: Constraints on the geometry of the L'Aquila 2009 seismogenic fault system. *Ital. J. Geosci.* **2012**, *131*, 330–347. [CrossRef]
11. Lavecchia, G.; Bello, S.; Andrenacci, C.; Cirillo, D.; Ferrarini, F.; Vicentini, N.; de Nardis, R.; Roberts, G.; Brozzetti, F. QUaternary fault strain INdicators database-QUIN 1.0-first release from the Apennines of central Italy. *Sci. Data* **2022**, *9*, 204. [CrossRef] [PubMed]
12. Falini, F. *Notizie Preliminari sui Lavori di Rilevamento di Dettaglio dalle Caratteristiche del Giacimento Lignitifero del Mercure (Provincie di Potenza e Cosenza)*; Convegno-Mostra Nazionale delle Ligniti; Multilith dalla Siderea: Rome, Italy, 1955.
13. GEMINA. Il bacino del Mercure. In *Ligniti e Torbe Dell'Italia Continentale*; Ilte: Torino, Italy, 1963; pp. 137–156.
14. Giaccio, B.; Galli, P.; Peronace, E.; Arienzo, I.; Nomade, S.; Cavinato, G.P.; Mancini, M.; Messina, P.; Sottili, G. A 560–440 ka tephra record from the Mercure Basin, southern Italy: Volcanological and tephrostratigraphic implications. *J. Quat. Sci.* **2014**, *29*, 232–248. [CrossRef]
15. Schiattarella, M.; Torrente, M.; Russo, F.; Analisi strutturale ed osservazioni morfostratigrafiche nel bacino del Mercure (confine calabro-lucano). *Il Quat. Ital. J. Quat. Sci.* **1994**, *7*, 613–626.
16. Ercoli, M.; Cirillo, D.; Pauselli, C.; Jol, H.M.; Brozzetti, F. Ground-penetrating radar signature of Quaternary faulting: A study from the Mt. Pollino region, southern Apennines, Italy. *Solid Earth* **2021**, *12*, 2573–2596. [CrossRef]
17. Robustelli, G.; Ermolli, E.R.; Petrosino, P.; Jicha, B.; Sardella, R.; Donato, P. Tectonic and climatic control on geomorphological and sedimentary evolution of the Mercure basin, southern Apennines, Italy. *Geomorphology* **2014**, *214*, 423–435. [CrossRef]
18. Galli, P.; Molin, D.; Camassi, R.; Castelli, V. Il terremoto del 9 settembre 1998 nel quadro della sismicità storica del confine calabro-lucano. Possibili implicazioni sismotettoniche. *Il Quat. Ital. J. Quat. Sci.* **2001**, *14*, 31–40.
19. Cinti, F.R.; Cucci, L.; Pantosti, D.; D'Addezio, G.; Meghraoui, M. A major seismogenic fault in a 'silent area': The Castrovillari fault (southern Apennines, Italy). *Geophys. J. Int.* **1997**, *130*, 595–605. [CrossRef]
20. Cinti, F.; Moro, M.; Pantosti, D.; Cucci, L.; D'addezio, G. New constraints on the seismic history of the Castrovillari fault in the Pollino gap (Calabria, southern Italy). *J. Seismol.* **2002**, *6*, 199–217. [CrossRef]
21. Knott, S.D. The Liguride complex of southern Italy—A Cretaceous to Paleogene accretionary wedge. *Tectonophysics* **1987**, *142*, 217–226. [CrossRef]
22. Tangari, A.C.; Scarciglia, F.; Piluso, E.; Marinangeli, L.; Pompilio, L. Role of weathering of pillow basalt, pyroclastic input and geomorphic processes on the genesis of the Monte Cerviero upland soils (Calabria, Italy). *CATENA* **2018**, *171*, 299–315. [CrossRef]
23. Monaco, C.; Tortorici, L. Tectonic role of ophiolite-bearing terranes in the development of the Southern Apennines orogenic belt. *Terra Nova* **1995**, *7*, 153–160. [CrossRef]
24. Filice, F.; Liberi, F.; Cirillo, D.; Pandolfi, L.; Marroni, M.; Piluso, E. Geology map of the central area of Catena Costiera: Insights into the tectono-metamorphic evolution of the Alpine belt in Northern Calabria. *J. Maps* **2015**, *11*, 114–125. [CrossRef]

25. Marinangeli, L.; Pompilio, L.; Baliva, A.; Billotta, S.; Bonanno, G.; Domeneghetti, M.C.; Fioretti, A.M.; Menozzi, O.; Nestola, F.; Piluso, E.; et al. Development of an ultra-miniaturised XRD/XRF instrument for the in situ mineralogical and chemical analysis of planetary soils and rocks: Implication for archaeometry. *Rend. Lincei* **2015**, *26*, 529–537. [CrossRef]
26. Bethke, C.; Yeakel, S. *The Geochemist's Workbench Release 7.0—Essentials Guide*; Hydrogeology Program, University of Illinois: Urbana, IL, USA, 2008.
27. Shvarov, Y.V. HCh: New potentialities for the thermodynamic simulation of geochemical systems offered by Windows. *Geochem. Int.* **2008**, *46*, 834. [CrossRef]
28. Cleverley, J.S.; Bastrakov, E.N. K2GWB: Utility for generating thermodynamic data files for the Geochemist's Workbench® at 0–1000 C and 1–5000 bar from UT2K and the UNITHERM database. *Comput. Geosci.* **2005**, *31*, 756–767. [CrossRef]
29. Robie, R.A.; Huebner, J.S.; Hemingway, B.S. Heat capacities and thermodynamic properties of braunite (Mn7SiO12) and rhodonite (MnSiO3). *Am. Mineral.* **1995**, *80*, 560–575. [CrossRef]
30. Jacob, K.; Kumar, A.; Waseda, Y. Gibbs energy of formation of MnO: Measurement and assessment. *J. Phase Equilibria Diffus.* **2008**, *29*, 222–230. [CrossRef]
31. Jacob, K.; Kumar, A.; Rajitha, G.; Waseda, Y. Thermodynamic data for mn3o4, mn2o3 and mno2. *High Temp. Mater. Process.* **2011**, *30*, 459–472. [CrossRef]
32. Wolery, T.W.; Jarek, R.L. Software user's manual. *EQ3/6 Version* **2003**, *8*, 376.
33. Roine, A. *HSC Chemistry® 7.0 User's Guide–Volume* 1/2*–Chemical Reaction and Equilibrium Software with Extensive Thermochemical Database and Flowsheet Simulation*; Outotec Information Center: Pori, Finland, 2009.
34. Blanc, P.; Lassin, A.; Piantone, P.; Burnol, A. *Thermoddem a Database Devoted to Waste Minerals*; Bureau de Recherches Géologiques et Minieres (Orléans, France): Orléans, France, 2007.
35. Johnson, J.W.; Oelkers, E.H.; Helgeson, H.C. SUPCRT92: A software package for calculating the standard molal thermodynamic properties of minerals, gases, aqueous species, and reactions from 1 to 5000 bar and 0 to 1000 C. *Comput. Geosci.* **1992**, *18*, 899–947. [CrossRef]
36. Post, J.E. Manganese oxide minerals: Crystal structures and economic and environmental significance. *Proc. Natl. Acad. Sci. USA* **1999**, *96*, 3447–3454. [CrossRef] [PubMed]
37. Potter, R.M.; Rossman, G.R. Mineralogy of manganese dendrites and coatings. *Am. Mineral.* **1979**, *64*, 1219–1226.
38. Robb, L. *Introduction to Ore-Forming Processes*; John Wiley & Sons: Hoboken, NJ, USA, 2020.
39. Sibson, R.H. Arterial faults and their role in mineralizing systems. *Geosci. Front.* **2019**, *10*, 2093–2100. [CrossRef]
40. Spencer, J.E.; Welty, J.W. Possible controls of base-and precious-metal mineralization associated with Tertiary detachment faults in the lower Colorado River trough, Arizona and California. *Geology* **1986**, *14*, 195–198. [CrossRef]
41. Calegari, S.S.; Aiolfi, T.R.; Neves, M.A.; Soares, C.C.V.; Marques, R.d.A.; Caxito, F.d.A. Filling materials in brittle structures as indicator of Cenozoic tectonic events in Southeastern Brazil. *Anu. Inst. Geociencias* **2020**, *43*, 237–254. [CrossRef]
42. Jones, S.; McNaughton, N.J.; Grguric, B. Structural controls and timing of fault-hosted manganese at Woodie Woodie, East Pilbara, Western Australia. *Ore Geol. Rev.* **2013**, *50*, 52–82. [CrossRef]
43. Krauskopf, K.B. Separation of manganese from iron in sedimentary processes. *Geochim. Cosmochim. Acta* **1957**, *12*, 61–84. [CrossRef]
44. Hewett, D. Manganite, hausmannite, braunite; features, modes of origin. *Econ. Geol.* **1972**, *67*, 83–102. [CrossRef]
45. Julien, C.; Massot, M.; Poinsignon, C. Lattice vibrations of manganese oxides: Part I. Periodic structures. *Spectrochim. Acta Part Mol. Biomol. Spectrosc.* **2004**, *60*, 689–700. [CrossRef]
46. Vermeersch, E.; Košek, F.; De Grave, J.; Jehlička, J.; Vandenabeele, P.; Rousaki, A. Identification of tunnel structures in manganese oxide minerals using micro-Raman spectroscopy. *J. Raman Spectrosc.* **2023**, *54*, 1201–1212. [CrossRef]
47. Vermeersch, E.; Košek, F.; De Grave, J.; Jehlička, J.; Rousaki, A. Layered manganese oxides structures: Micro-Raman and selected mobile Raman spectroscopic studies. *J. Raman Spectrosc.* **2024**, *55*, 246–262. [CrossRef]
48. McKeown, D.A.; Post, J.E. Characterization of manganese oxide mineralogy in rock varnish and dendrites using X-ray absorption spectroscopy. *Am. Mineral.* **2001**, *86*, 701–713. [CrossRef]
49. Mc Kenzie, R.M. Manganese oxides and hydroxides. *Miner. Soil Environ.* **1989**, *1*, 439–465. [CrossRef]
50. Comodi, P.; Nazzareni, S.; Zanazzi, P.F.; Speziale, S. High-pressure behavior of gypsum: A single-crystal X-ray study. *Am. Mineral.* **2008**, *93*, 1530–1537. [CrossRef]
51. Nazzareni, S.; Comodi, P.; Bindi, L.; Garbarino, G.; Bobrov, A. Equation of state of Fe 3+-bearing phase-X. *Phys. Chem. Miner.* **2012**, *39*, 553–559. [CrossRef]
52. Yun, S.; Hwang, H.; Hwang, G.; Kim, Y.; Blom, D.; Vogt, T.; Post, J.E.; Jeon, T.Y.; Shin, T.J.; Zhang, D.Z.; et al. Super-hydration and reduction of manganese oxide minerals at shallow terrestrial depths. *Nat. Commun.* **2022**, *13*, 1942. [CrossRef]
53. Tutti, F.; Dubrovinsky, L.S.; Saxena, S.K.; Carlson, S. Stability of KAlSi3O8 Hollandite-type structure in the Earth's lower mantle conditions. *Geophys. Res. Lett.* **2001**, *28*, 2735–2738. [CrossRef]
54. Galli, P.; Galadini, F.; Pantosti, D. Twenty years of paleoseismology in Italy. *Earth-Sci. Rev.* **2008**, *88*, 89–117. [CrossRef]
55. Bello, S.; Perna, M.G.; Consalvo, A.; Brozzetti, F.; Galli, P.; Cirillo, D.; Andrenacci, C.; Tangari, A.C.; Carducci, A.; Menichetti, M.; et al. Coupling rare earth element analyses and high-resolution topography along fault scarps to investigate past earthquakes: A case study from the Southern Apennines (Italy). *Geosphere* **2023**, *19*, 1348–1371. [CrossRef]
56. Marchesini, M.; Pagano, R. The Val Graveglia manganese district, Liguria, Italy. *Mineral. Rec.* **2001**, *32*, 349.

57. Mongelli, G.; Critelli, S.; Dinelli, E.; Paternoster, M.; Perri, F. Mn-and Fe-carbonate rich layers in Meso-Cenozoic shales as proxies of environmental conditions: A case study from the southern Apennine, Italy. *Geochem. J.* **2010**, *44*, 211–223. [CrossRef]
58. Caine, J.S.; Bruhn, R.L.; Forster, C.B. Internal structure, fault rocks, and inferences regarding deformation, fluid flow, and mineralization in the seismogenic Stillwater normal fault, Dixie Valley, Nevada. *J. Struct. Geol.* **2010**, *32*, 1576–1589. [CrossRef]
59. Sibson, R.; Moore, J.M.M.; Rankin, A. Seismic pumping—A hydrothermal fluid transport mechanism. *J. Geol. Soc.* **1975**, *131*, 653–659. [CrossRef]
60. Salvioli-Mariani, E.; Boschetti, T.; Vescovi, F.M.; Scacchetti, M.; Toscani, L.; Mattioli, M. Hydrothermal lead-zinc-copper mineralizations in sedimentary rocks of Northern Apennines (Italy). *J. Geochem. Explor.* **2024**, *257*, 107365. [CrossRef]
61. Hönisch, B.; Ridgwell, A.; Schmidt, D.N.; Thomas, E.; Gibbs, S.J.; Sluijs, A.; Zeebe, R.; Kump, L.; Martindale, R.C.; Greene, S.E.; et al. The geological record of ocean acidification. *Science* **2012**, *335*, 1058–1063. [CrossRef]
62. Napolitano, F.; Gabrielli, S.; De Siena, L.; Amoroso, O.; Capuano, P. Imaging overpressurised fracture networks and geological barriers hindering fluid migrations across a slow-deformation seismic gap. *Sci. Rep.* **2023**, *13*, 19680. [CrossRef]
63. Smeraglia, L.; Bernasconi, S.M.; Berra, F.; Billi, A.; Boschi, C.; Caracausi, A.; Carminati, E.; Castorina, F.; Doglioni, C.; Italiano, F.; et al. Crustal-scale fluid circulation and co-seismic shallow comb-veining along the longest normal fault of the central Apennines, Italy. *Earth Planet. Sci. Lett.* **2018**, *498*, 152–168. [CrossRef]
64. Talone, D.; De Siena, L.; Lavecchia, G.; de Nardis, R. The Attenuation and Scattering Signature of Fluid Reservoirs and Tectonic Interactions in the Central-Southern Apennines (Italy). *Geophys. Res. Lett.* **2023**, *50*, e2023GL106074. [CrossRef]
65. de Nardis, R.; Vuan, A.; Carbone, L.; Talone, D.; Romano, M.A.; Lavecchia, G. Interplay of tectonic and dynamic processes shaping multilayer extensional system in southern-central Apennines. *Sci. Rep.* **2024**, *14*, 18375. [CrossRef]
66. Long, K. Descriptive model of detachment-fault-related mineralization. *Dev. Miner. Depos. Model. Geol. Surv. Bull.* **1992**, *2004*, 57–62.